NANO LETTERS

2009
Vol. 9, No. 7
2553-2558

Mid-IR Plasmonics: Near-Field Imaging of Coherent Plasmon Modes of Silver Nanowires

Andrew C. Jones,[†,‡] Robert L. Olmon,[‡,§] Sara E. Skrabalak,[||] Benjamin J. Wiley,[⊥] Younan N. Xia,[#] and Markus B. Raschke*[,†,‡]

Department of Physics, Department of Electrical Engineering, and Department of Chemistry, University of Washington, Seattle, Washington 98195, Department of Chemistry, University of Indiana, Bloomington, Indiana 47405-7102, Department of Chemistry, Harvard University, Cambridge, Massachusetts 02138, and Department of Biomedical Engineering, Washington University, St. Louis, Missouri 63130

Received February 26, 2009; Revised Manuscript Received May 6, 2009

ABSTRACT

Chemically synthesized metallic nanostructures can exhibit a strong local optical field enhancement associated with their high degree of crystallinity and well-defined geometry-dependent surface plasmon resonances. The extension of the plasmon modes into the mid-IR spectral range (3−30 μm) is shown for micrometer-sized nanowires with high aspect ratios available in the form of pentagonally twinned Ag crystallites as grown by polyol synthesis. Using scattering-scanning near-field optical microscopy, the associated IR plasmon modes are identified, and their underlying spatial distribution and enhancement of the optical polarization density is measured via phase, amplitude, and polarization resolved optical vector-field mapping. The transition from dipolar to multipolar resonances is observed and described by modeling the Ag wires using a modified cylindrical waveguide theory. For 10.6 μm excitation, dipole antenna resonances are observed at a resonant length of $L = \lambda_{eff}/2$ with $\lambda_{eff} \approx 10.6\ \mu m/(1.8 \pm 0.5) \approx 6 \pm 2\ \mu m$. This effective wavelength scaling is the result of electronic damping, despite the high aspect ratios of the wires of order 1:10 to 1:200. With the optical cycle period τ_{IR} being comparable to the Drude relaxation time of $\tau \sim 40$ fs the mid-IR defines the low-energy limit of the coherent plasmon regime ($\tau_{IR} \lesssim \tau$) at the transition to purely geometric antenna resonances ($\tau_{IR} > \tau$).

Introduction. Phenomena and applications involving electromagnetic surface waves of noble metals encompass a wide frequency range extending over many orders of magnitude only limited at high energies by the interband absorption typically in the blue/UV spectral range as determined by the electronic band structure of the metal. At optical frequencies, the resonant surface bound excitation of surface plasmon polaritons (SPP) of thin metallic films and individual or coupled metallic nanostructures is associated with a coherent resonant oscillation of conduction electrons at the interface of the metal and its dielectric surrounding. This resonance is size and shape dependent which allows for control of optical fields on the nanometer scale through the manipulation of the material and geometric parameters of the particle.[1−4]

In contrast to the visible spectral region, the intrinsic properties of surface waves in the mid-IR regime are less well understood. This is despite the general importance of mid-IR active nanostructures for surface-enhanced IR absorption (SEIRA),[5−10] as optical antennas for IR emitters,[11−13] IR and THz detectors,[14] and thermal sensors.[15,16] Due to the strong damping of the coherent electron oscillation at visible frequencies, the corresponding SPP propagation length is limited to several micrometers.[17−19] The damping is greatly reduced in the IR allowing propagation lengths into the millimeter range.[20] In addition, studying the mid-IR response of metal nanostructures provides microscopic insight into the underlying electron dynamics with the optical cycle period in that wavelength range being comparable to the Drude electronic relaxation time τ. This spectral range signifies the transition regime that links the low-energy Hagen−Rubens regime describing classical antenna resonances ($\omega \ll \tau^{-1}$) with the relaxation regime ($\tau^{-1} < \omega < \omega_{pl}$) of the surface plasmon, with ω_{pl} being the plasma frequency of the metal.[21]

The ability to tune the optical response of metallic nanostructures through the manipulation of their geometry[4] has greatly improved with the development of chemical

* Corresponding author, raschke@chem.washington.edu.
[†] Department of Physics, University of Washington.
[‡] Department of Chemistry, University of Washington.
[§] Department of Electrical Engineering, University of Washington.
[||] Department of Chemistry, University of Indiana.
[⊥] Department of Chemistry, Harvard University.
[#] Department of Biomedical Engineering, Washington University.

10.1021/nl900638p CCC: $40.75
Published on Web 06/05/2009

synthetic methods to produce crystalline metal nanostructures with structural control down to the nanometer range.[22−26] On that basis, the synthesis of quasi-one-, two-, and three-dimensional nanoparticles with sizes in the 10s to 100s nm range provides access to plasmon resonances throughout the visible and near-IR spectral region.[5,27,28]

The synthesis of silver nanowires with lengths up to tens of micrometers allows for the extension of structural resonances into the mid-IR range. These wires can be grown with high yield by reducing silver nitrate with ethylene glycol in the presence of poly(vinyl pyrrolidone).[29] A homogeneous diameter even for high aspect ratios (1:10 to 1:200), an atomically smooth surface, and reduced electron scattering with the absence of grain boundaries due to the crystalline structure enables an improvement of the optical properties relative to rough, polycrystalline wires made from electrothermal deposition thus providing an ideal material for mid-IR plasmonics.

With previous work having been limited to the study of the far-field properties of related crystalline structures,[30] little is yet known as to the nature of the underlying resonant modes and associated spatial field distribution and local field enhancements resulting from plasmonic excitations in the mid-IR range. To address these questions, here, we study resonant dipole and higher order modes at the low energy limit of the coherent plasmon polariton regime of these chemically synthesized crystalline Ag nanowires. Phase sensitive optical vector near-field mapping at an excitation wavelength of $\lambda = 10.6\ \mu$m by scattering-scanning near-field optical microscopy (*s*-SNOM) provides a direct image of the nanometer scale spatial field distribution of the surface standing waves and their dependence on microscopic structural parameters. The scaling of the dipolar resonance with wavelength could be established as predicted theoretically, occurring for lengths shorter than the classical $\lambda/2$ antenna resonance. This deviation from the classical prediction is primarily due to the finite skin depth, wire thickness, and the surrounding dielectric.[31−33] In addition, our results provide the near-field enhancement and its distribution underlying, e.g., recent SEIRA observations using related geometries produced lithographically.[9,10,34]

Experiment. The Ag nanowires were synthesized as described in detail previously.[29] Five milliliters of ethylene glycol (EG) were stirred in a glass vial, suspended in an oil bath (150 °C). After the EG was heated for 1 h under stirring at 260 rpm, 40 μL of a 4 mM copper(II) chloride solution ($CuCl_2$) in EG was added. After an additional 15 min, 1.5 mL of a 0.147 M poly(vinyl-pyrrolidone) (PVP, molecular weight $M_w \approx 55000$, concentration expressed in terms of monomer) solution in EG was added followed immediately by 1.5 mL of a 0.094 M silver nitrate ($AgNO_3$) solution in EG. The reaction was quenched after another 1 h. The reaction products were washed with acetone, collected by centrifugation, and subsequently dispersed in water. The silver nanowires obtained were characterized by scanning and transmission electron microscopy (SEM/TEM) as shown in panels b−d of Figure 1. They exhibit a pentagonal cross section due to 5-fold twinning consistent with silver nanowires grown from decahedral seeds in which the (100) surfaces of the wire have been stabilized with PVP.[26,35]

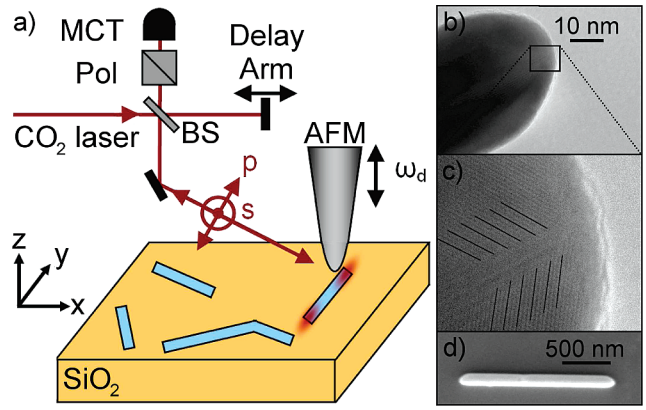

Figure 1. Scattering-scanning near-field optical microscopy (*s*-SNOM) (a) with polarization-selective excitation and interferometric homodyne detection to probe specific near-field vector components of IR plasmon modes of Ag nanowires. Transmission electron microscope images (TEM) confirm the crystalline nature and pentagonal twinning of the nanowires (b, c). Solid lines parallel to the atomic planes have been added as a guide to the eye. Scanning electron microscope (SEM) image of a representative Ag nanowire with typical aspect ratio studied (d).

The experimental setup, as shown schematically in Figure 1 a, is based on a modified atomic force microscope (AFM, CP-Research, Veeco Inc.) with sample scanning and dynamic force control of the cantilever probe tip.[36,37] A CO_2 laser, $\lambda = 10.6\ \mu$m, is used as a light source for mid-IR optical excitation in an epi-illumination and -detection geometry. A Cassegrain objective (NA = 0.5) at an angle of 70° with respect to the surface normal is used to focus the light onto the tip apex region with an elliptical focus size of $\approx 30\ \mu$m in width with incident power of approximately 5 mW. Polarizing optics control the incident and detected light polarizations with s and p defined with respect to the plane formed by the incidence/emission k-vector and the AFM tip axis (see Figure 1). Individual Ag wires near the expected resonant length are located via topographic scans. The tip-scattered near-field response of a wire is then recorded simultaneously with the AFM topography using an MCT detector (Kolmar, model KLD-0.25/DC/11.5). Pt-coated AFM probes (Veeco OSCM-Pt and Nanosensors ATEC-NCPt) with forward pointing tips to facilitate illumination and detection using the external optics are used to perform the *s*-SNOM measurements.[38]

The near-field signal from the Ag nanowires is discriminated against the tip-scattered far-field background by demodulation at the second-harmonic of the tip sample dither frequency $2\omega_d$.[39,40] Optical phase information is obtained by interferometric homodyne detection using a modified implementation compared to previous methods[40−42] as will be discussed below. For probing specific vector near-field components, selective s- and p-polarized excitation and detection is applied (Figure 1). This polarization selective detection together with knowledge of the phase information characterizes the local field distribution associated with the plasmon modes of the nanowires.

It should be noted that due to the AFM cantilever oscillation, the *s*-SNOM signal represents a map of the gradient of the optical near-field; however, due to the evanescent character of the near-field, strong gradients in general correspond to regions of high field intensity. As the *s*-SNOM mapping of the optical field surrounding the Ag nanowires represents the near-field intensity gradient within $\approx$ 30 nm above the metal surface, it is thus a measure of the optical surface polarization density of the standing surface plasmon wave with the related strong spatial field confinement at the ends of the wires.

Optical Vector Near-Field Mapping. Full characterization of the spatial near-field distribution surrounding the metal nanoparticles entails the measurement of both amplitude and phase of the electric field components in all three Cartesian coordinates.[36,37,43,44] Here, we restrict our measurements to the E_z field which is the field component predominately probed under selective p-polarized detection, p_{out} (see Figure 1).[45,37] Characterization of E_z is most valuable for the identification of the mode behavior of the plasmonic resonance in Ag wires as it is associated with a phase change of the induced SPP polarization density at the poles. Furthermore, for s-polarized excitation and cross-polarized detection of p-polarized scattered light, $s_{in}p_{out}$, the tip−sample coupling as well as the self-homodyne field are minimized thus reducing the risk for imaging artifacts.

The amplitude of a signal observed for a given excitation/detection polarization combination can be understood through the use of the tip-scattering tensor given by

$$\mathcal{F} = \begin{pmatrix} 0 & 0 & 0 \\ 0 & F_{ss} & F_{sp} \\ 0 & F_{ps} & F_{pp} \end{pmatrix} \quad (1)$$

with coefficients F_{jk} representing the tip scattering efficiency, and the indices j and k the detected and incident s and p polarizations. Here, the F_{sp} and F_{ps} tensor elements represent the scattering efficiencies for the cross-polarized excitation and detection experimental configurations $p_{in}s_{out}$ and $s_{in}p_{out}$, respectively. For example, for the case of a nanowire oriented parallel with respect to the *y*-axis E_z is predominately detected for the $s_{in}p_{out}$ polarization combination (Figure 1).

In general for $p_{in}p_{out}$, the far-field background is of the same polarization as the signal of interest which can lead to interferometric self-homodyne phase contrast. This contrast may be utilized to gain useful information under certain conditions. Depending on the relative (but uncontrolled) phase of the far-field backscattered signal from the tip and sample roughness with respect to the phase of the local tip-scattered near-field plasmon emission, a phase contrast is observed provided that the far-field contribution is of comparable magnitude to the near-field strength.

For (controlled) phase-resolved *s*-SNOM imaging, interferometric homodyne detection is employed by adjusting the reference field to a desired phase and amplitude. The near-field emission from respective poles oscillating out of phase with respect to one another for a resonant mode is superimposed with the reference field of specific phase, leading to constructive and destructive interference, respectively. This provides relative phase information between the different poles of dipole and multipole plasmon excitation.

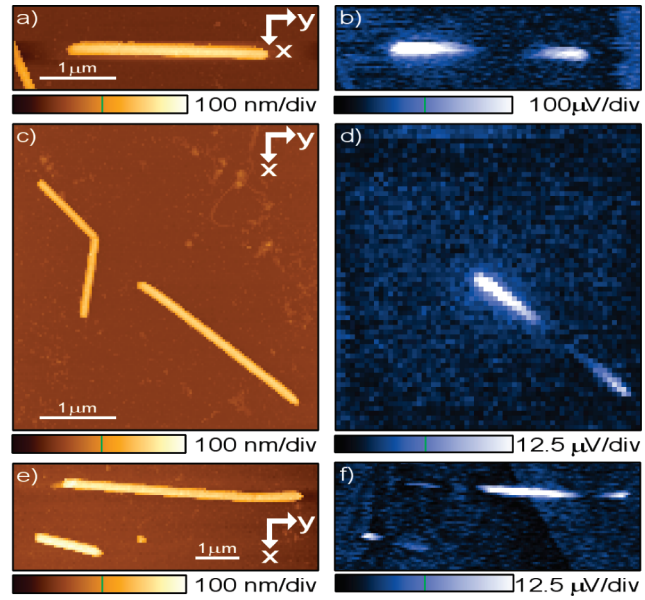

Figure 2. Topography (a, c, and e) and corresponding nonphase resolved near-field IR *s*-SNOM $|E_z|^2$ signal (b, d, and f) for $s_{in}p_{out}$ polarization configuration for crystalline Ag wires of different lengths. For lengths up to $L \approx 4$ μm the Ag wires exhibit a dipolar mode, with multipolar resonances supported for longer wire lengths (f).

In contrast to other methods where the amplitude of the field in the reference arm is much greater than the scattered near-field signal,[40,42] in our approach of weak interferometric homodyne amplification the reference amplitude is chosen to be comparable to that of the near-field signal. For an appropriately adjusted reference phase this approach results in fully constructive and destructive interference at respective out of phase poles of the particle resonance (see Supporting Information for further details). It further allows for a representation of both phase and amplitude information in one data set for a given optical near-field vector component. Also, in general, the weak homodyne amplification can be advantageous in determining the optical signal phase using broad-band excitation; the constructive and destructive interference in the interferogram yields both spectral and relative phase information.

Results. Figure 2 displays topography and nonphase-resolved *s*-SNOM scans corresponding to $|E_z|^2$ of different Ag wires under the $s_{in}p_{out}$ illumination and detection configuration. Lengths of Ag nanowires range from $L \approx 1$ μm to $L \approx 12.3$ μm. For lengths up to approximately 4 μm, dipolar mode patterns are observed (Figure 2, panels b and d) with one lobe at either end of the wire. For longer wires, $L \approx 6$ μm (upper wire in panel f of Figure 2), the wires exhibit a more complex spatial distribution characteristic of multipolar excitations.

No contrast is observed for sufficiently off-resonant excitation as evident by the lack of optical signal, panels b and d of Figure 2, corresponding to several structural features seen in the topographies in (a) and (c). For wires oriented

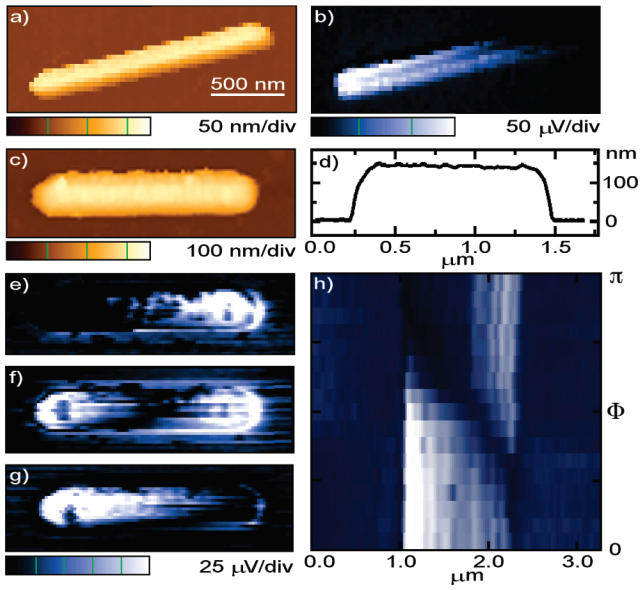

Figure 3. Topography (a) and corresponding *s*-SNOM signal (b) for a typical Ag wire under the influence of a self-homodyne field. The phase relation between the poles of a Ag wire is demonstrated by topography (c and d) with corresponding detected *s*-SNOM signal under interferometric homodyne amplification (e−h). Contrast arises from constructive and destructive interference of the reference field with out-of-phase field from the respective poles of the wire. E_z *s*-SNOM scans for discrete reference phase values of $\Phi = \pi$, $\pi/2$, and 0 (e, f, and g, respectively). Corresponding background subtracted *s*-SNOM line scans for continuous variation of Φ (h).

predominantly along the *x* direction (wire section visible on left side of (a), the longitudinal resonance cannot be excited for s_{in}. Similarly, negligible contrast is observed for submicrometer Ag particles that exhibit plasmon resonance in the visible spectral region. The bent wire shown in (c) does not exhibit any *s*-SNOM contrast although the driving field in the *y*-direction still has a component along the upper wire segment. This may be due to an associated spectral resonance shift and/or additional damping associated with the bend itself.

Panels a and b of Figure 3 display corresponding AFM and *s*-SNOM data taken under the $p_{in}p_{out}$ configuration exhibiting self-homodyne interference contrast. The observed contrast arises from the constructive (left) and destructive (right) interference of the nanowire signal with the uncontrolled self-homodyne field provided by the far-field background as discussed above. Panels e through h show results for homodyne detection under controlled interferometric phase and amplitude reference conditions. Panels c and d display the topography of a wire of length, $l \approx 1.25$ μm exhibiting a dipolar resonance. Corresponding optical *s*-SNOM scans representing E_z are shown in (e−g) for relative phases of the homodyne signal of $\Phi = \pi$, $\pi/2$, and 0, respectively. Figure 3h shows the signal variation for a line scan along the center of the wire incrementally varying the phase between $\Phi = 0$ and π. The inversion of the signal contrast at the two nanowire ends varying the reference phase is characteristic for the dipole excitation. Further details describing the nature of the observed signal are discussed in the Supporting Information.

Discussion. In the following we discuss several implications of the results above. On the basis of spectral response and theory, a large SEIRA effect as observed on structurally related micrometer sized metal nanowires was attributed to strong local-field enhancement at the poles.[10] The *s*-SNOM images in Figures 2 and 3 agree with these predictions with the highest observed optical intensities occurring near the ends of the Ag wires as expected. Our measurements only provide a rough estimate of the local field enhancement with values of order 10−50 as deduced from comparison with the detected signal from the unenhanced center of the wire and the estimate of an enhancement of unity around the noise level. This enhancement is consistent with a theoretical value of 45, calculated 1 nm above the surface for Ag wires at their dipole resonance in the 3.5 μm wavelength range.[10]

Estimate of Resonant Length. From the study of Ag wires of different lengths, a dipolar field pattern is observed for wires between $L \approx 1$ μm and $L \approx 4$ μm. A resonant length of $L_{dipole} \simeq 3$ μm could be deduced for the $\lambda = 10.6$ μm wavelength excitation used. This length is considerably shorter than the first ideal classical antenna resonance at $L \approx \lambda/2 = 5.3$ μm. Despite high aspect ratios of 1:10 to 1:200, an inhomogeneous dielectric environment and still considerable damping (even at mid-IR frequencies) give rise to a departure from the ideal scattering behavior of perfectly conducting and infinitely thin metal wires in which the antenna resonances occur at lengths of $L \approx n\lambda/2$ for $n = 1, 2, 3,...$.[46]

Within the low frequency limit, linear antenna resonances are dictated by the approximation that the radius *r* is much smaller than the wavelength (i.e., $r \ll \lambda$) but is still much greater than the skin depth δ. In this frequency range, the optical properties of metals are largely frequency independent and characterized by both a large real conductivity σ_{Re} and low absorption coefficient $\alpha = 2/\delta$.

The extension of linear antenna structures to the infrared/visible spectral range typically results in structure sizes in which the skin depth is comparable to the radius of the antenna, i.e., $\delta \sim r$. This is the case for our chemically synthesized Ag wires with radii down to $r \approx 25$ nm and skin depth $\delta \approx 30$ nm at $\lambda = 10.6$ μm.[47] Here, the electric field significantly penetrates into the antenna structure resulting in a deviation of the optical properties from that of classical antenna theory which is reflected in the modification of the half-dipole resonance length.[21]

Recently, a modified classical waveguide theory for the TM modes of a cylindrical waveguide[48] which accounts for the reactance of the ends of the antennas was used to predict the effective wavelength scaling behavior for optical antennas.[33] This theory and other models, which incorporate DDA and boundary element methods,[31,32] predict a scaling behavior that has been confirmed by infrared spectroscopy in lithographically grown structures[9,34] and comparison of *s*-SNOM and numerical simulations of optical infrared antenna structures.[37]

Using the modified waveguide theory[33] and assigning an effective real dielectric constant equal to the geometric average of the dielectric constants for the SiO_2 substrate and

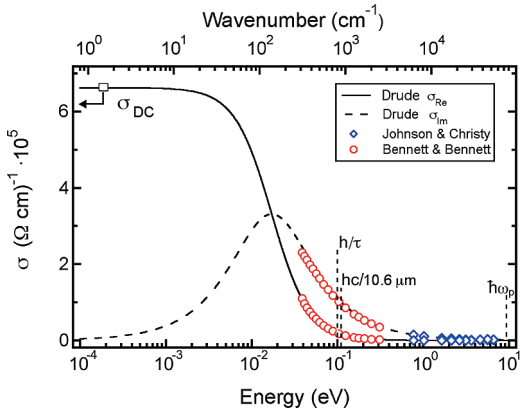

Figure 4. Drude model prediction of the frequency dependence of the real (solid line) and imaginary (dashed line) conductivity of silver. Selected data points up to the longest wavelength available from ref 47, derived from measured optical constants of silver, illustrate the close correspondence between Drude theory ($\tau = 40$ fs, $\hbar\omega_{pl} = 8.98$ eV, and $\epsilon_{DC} = 3.7$) and experiment in the mid-IR and visible spectral ranges.[47,49,50]

air, $\epsilon_{surr} = (\epsilon_{air}\epsilon_{sub})^{1/2} \approx 2$, we derive an effective wavelength of $\lambda_{eff} \approx 6.7$ μm and half wavelength resonance of $L_{dipole} \approx 3.4$ μm for a typical Ag wire of radius $r = 25$ nm for incident light $\lambda = 10.6$ μm. This result is in good agreement with our experimental findings of $L_{dipole} \simeq 3$ μm which corresponds to $\lambda_{eff} \approx 10.6$ μm/$(1.8 \pm 0.5) \approx 6 \pm 2$ μm.

Dephasing Time and Plasmon Properties in the IR. Planar SPPs in the visible are characterized by both a distinct dispersion relation with respect to the light line and a high degree of field localization near the surface resulting from a nonzero in-plane component of the electric field which permits the formation of a spatially and temporally varying charge distribution. These properties reflect the fact that the visible frequency range corresponds to the upper limit of the relaxation regime, $1/\tau \sim \omega < \omega_{pl}$.[21] Here, unlike the low frequency limit, the optical properties of metals are marked by both real and imaginary conductivities σ_{Re} and σ_{Im}, respectively, as well as a related large absorption coefficient α. Visible frequencies, in particular, are distinguished by a low σ_{Im} and a negligible σ_{Re} which is reflected in the heavy loss and low propagation lengths for visible plasmon excitations.[18,19]

While the mid-IR and visible spectral ranges both fall into what is generally classified as the relaxation regime,[21] these two spectral ranges are distinct in their optical material responses. Figure 4 illustrates these inherent differences as manifested in σ_{Re} and σ_{Im} for a simple Drude description of the optical properties of silver.[47,50,49] At lower frequencies in the relaxation regime (the mid-IR spectral range) metals exhibit appreciable values of σ_{Re} and σ_{Im}. While α is expected to retain a relatively constant high value for frequencies throughout the entire relaxation regime ($\alpha \approx 7.7 \times 10^5$, 9.0×10^5, and 8.5×10^5 cm^{-1}, for $\lambda = 0.5$, 10, and 30 μm, respectively), the enhanced conductivity relative to visible frequencies results in a reduction of loss and increase of the predicted propagation length l in the IR spectral range ($l \approx 16$ μm and 55 mm for an Ag/air interface at $\lambda = 0.5$ and 10 μm, respectively).[18,19]

Of further physical importance for low-frequency plasmon properties is the relaxation time τ of the metal which under the Drude model represents the mean time between electron scattering events. The relaxation time is of particular interest at mid-IR frequencies where the optical cycle time τ_{IR} becomes comparable to τ. As a result, the mid-IR spectral range represents the low frequency limit for the coherent plasmon excitation. This further highlights the interest in the variation of the carrier density in materials (e.g., semiconductors) to control the plasmon dephasing time τ.[51]

Summary. As they are associated with enhanced conductivity, plasmonic metal structures in the infrared are able to take advantage of a reduced loss compared to visible frequencies. Furthermore, previous work has indicated that crystalline nanomaterials exhibit longer scattering times, extended propagation lengths, and reduced energy loss compared to their lithographic counterparts.[52,53] This difference is primarily attributed to an abatement of the electron scattering related to polycrystalline grain boundaries and nanometer surface roughness.

Although infrared surface waves in planar geometries are characterized by a decrease in near-surface field localization with increasing wavelength, for localized surface plasmons the field confinement is determined by the local geometry. Single crystalline nanowires with tunable width and length can thus serve as essential building blocks for the design of IR nanophotonic devices with functionalities that may exceed the performance of their visible counterparts in field-enhancement, propagation distance, tunability, and ease of structural control. Taking advantage of the underlying enhanced optical properties of metals in the mid-IR spectral region associated with the higher conductivity, this opens the door for the yet under explored field of IR plasmonics.

Acknowledgment. Funding from the National Science Foundation (NSF CAREER Grant CHE 0748226 and DMR-0451788) is greatly acknowledged as is support under a National Science Foundation Graduate Research Fellowship (A.C.J.).

Supporting Information Available: A semiquantitative model description of the experimental requirements for phase-resolved imaging of E_z using weak-field homodyne interferometric amplification. This material is available free of charge via the Internet at http://pubs.acs.org.

References

(1) Ozbay, E. *Science* **2006**, *311* (5758), 189–193.
(2) Maier, S. A.; Brongersma, M. L.; Kik, P. G.; Meltzer, S.; Requicha, A. A. G.; Atwater, H. A. *Adv. Mater.* **2001**, *13* (19), 1501.
(3) El-Sayed, M. A. *Acc. Chem. Res.* **2001**, *34* (4), 257–264.
(4) Kelly, K. L.; Coronado, E.; Zhao, L. L.; Schatz, G. C. *J. Phys. Chem. B* **2003**, *107* (3), 668–677.
(5) Lal, S.; Grady, N. K.; Kundu, J.; Levin, C. S.; Lassiter, J. B.; Halas, N. J. *Chem. Soc. Rev.* **2008**, *2* (4), 707–718.
(6) Leverette, C. L.; Jacobs, S. A.; Shanmukh, S.; Chaney, S. B.; Dluhy, R. A.; Zhao, Y. P. *Appl. Spectrosc.* **2006**, *60* (8), 906–913.
(7) Huo, S. J.; Xue, X. K.; Li, Q. X.; Xu, S. F.; Cai, W. B. *J. Phys. Chem. B* **2006**, *110* (51), 25721–25728.
(8) Le, F.; Brandl, D. W.; Urzhumov, Y. A.; Wang, H.; Kundu, J.; Halas, N. J.; Aizpurua, J.; Nordlander, P. *ACS Nano* **2008**, *2* (4), 707–718.

(9) Neubrech, F.; Kolb, T.; Lovrincic, R.; Fahsold, G.; Pucci, A.; Aizpurua, J.; Cornelius, T. W.; Toimil-Molares, M. E.; Neumann, R.; Karim, S. *Appl. Phys. Lett.* **2006**, *89* (25), 253104.
(10) Neubrech, F.; Pucci, A.; Cornelius, T. W.; Karim, S.; Garcia-Etxarri, A.; Aizpurua, J. *Phys. Rev. Lett.* **2008**, *101* (15), 157403.
(11) Greffet, J. J. *Science* **2005**, *308* (5728), 1561–1563.
(12) Yu, N. F.; Fan, J.; Wang, Q. J.; Pflugl, C.; Diehl, L.; Edamura, T.; Yamanishi, M.; Kan, H.; Capasso, F. *Nat. Photonics* **2008**, *2* (9), 564–570.
(13) Alu, A.; Engheta, N. *Nat. Photonics* **2008**, *2* (5), 307–310.
(14) Tang, L.; Kocabas, S. E.; , S.; Okyay, A. K.; Gagnon, D. S. L.; Saraswat, K. C.; Miller, D. A. B. *Nat. Photonics* **2008**, *2* (4), 226–229.
(15) Krenz, P.; Alda, J.; Boreman, G. D. *Infrared Phys. Technol.* **2008**, *51* (4), 340–343.
(16) Fumeaux, C.; Gritz, M. A.; Codreanu, I.; Schaich, W. L.; González, F. J.; Boreman, G. D. *Infrared Phys. Technol.* **2000**, *41* (5), 271–281.
(17) Bouhelier, A.; Wiederrecht, G. P. *Phys. Rev. B* **2005**, *71* (19), 195406.
(18) Raether, H. *Surface plasmons*, Springer: Berlin and New York, 1988.
(19) Maier, S. A. *Plasmonics: Fundamentals and Applications*; Springer: New York, 2007.
(20) Saxler, J.; Rivas, J. G.; Janke, C.; Pellemans, H. P. M.; Bolivar, P. H.; Kurz, H. *Phys. Rev. B* **2004**, *69* (15), 155427.
(21) Dressel, M. Gruner, G. *Electrodynamics of Solids*; Cambridge University Press: Cambridge and New York, 2002.
(22) Oldenburg, S. J.; Averitt, R. D.; Westcott, S. L.; Halas, N. J. *Chem. Phys. Lett.* **1998**, *288* (2−4), 243–247.
(23) Jana, N. R.; Gearheart, L.; Murphy, C. J. *Chem. Commun.* **2001**, (7), 617–618.
(24) Xia, Y.; Xiong, Y.; Lim, B.; Skrabalak, S. E. *Angew. Chem., Int. Ed.* **2009**, *48*, 60–103.
(25) Jin, R.; Cao, Y.; Mirkin, C.; Kelly, K. L.; Schatz, G. C.; Zheng, J. *Science* **2001**, *294*, 1901.
(26) Wiley, B. J.; Sun, Y. G.; Xia, Y. N. *Langmuir* **2005**, *21* (18), 8077–8080.
(27) Murphy, C. J.; San, T. K.; Gole, A. M.; Orendorff, C. J.; Gao, J. X.; Gou, L.; Hunyadi, S. E.; Li, T. *J. Phys. Chem. B* **2005**, *109* (29), 13857–13870.
(28) Wiley, B. J.; Im, S. H.; Li, Z.-Y.; McLellan, J.; Siekkinen, A.; Xia, Y. *J. Phys. Chem. B* **2006**, *110* (32), 15666–15675.
(29) Korte, K. E.; Skrabalak, S. E.; Xia, Y. *J. Mater. Chem.* **2008**, *18* (4), 437–441.
(30) Sando, G. M.; Berry, A. D.; Owrutsky, J. C. *J. Chem. Phys.* **2007**, *127*, 074705.
(31) Encina, E. R.; Coronado, E. A. *J. Phys. Chem. C* **2007**, *111* (45), 16796–16801.
(32) Bryant, G. W.; Garcia de Abajo, F. J.; Aizpurua, J. *Nano Lett.* **2008**, *8* (2), 631–636.
(33) Novotny, L. *Phys. Rev. Lett.* **2007**, *98* (26), 266802.
(34) Neubrech, F.; Weber, D.; Lovrincic, R.; Pucci, A.; Lopes, M.; Toury, T.; Lamy de La Chapelle, M. *Appl. Phys. Lett.* **2008**, *93* (16), 163105.
(35) Wiley, B.; Sun, Y.; Xia, Y. *Acc. Chem. Res.* **2007**, *40* (10), 1067–1076.
(36) Rang, M.; Jones, A. C.; Zhou, F.; Li, Z.-Y.; Wiley, B. J.; Xia, Y. N.; Raschke, M. B. *Nano Lett.* **2008**, *8* (10), 3357–3363.
(37) Olmon, R. L.; Krenz, P. M.; Jones, A. C.; Boreman, G. D.; Raschke, M. B. *Opt. Express* **2008**, *16* (25), 20295–20305.
(38) Silicon tips were also used with similar results, but with lower scattering efficiency, confirming no significant perturbation of intrinsic near-field distribution under investigation even for the strongly coupled $p_{in}p_{out}$ case.
(39) Esteban, R.; Vogelgesang, R.; Kern, K. *Phys. Rev. B* **2007**, *75* (19), 195410.
(40) Hillenbrand, R.; Keilmann, F. *Philos. Trans. R. Soc. London, Ser. A* **2004**, *362*, 787–805.
(41) Kim, Z. H.; Leone, S. R. *Opt. Express* **2008**, *16* (3), 1733–1741.
(42) Ocelic, N.; Huber, A.; Hillenbrand, R. *Appl. Phys. Lett.* **2006**, *89* (10), 101124.
(43) Gersen, H.; Novotny, L.; Kuipers, L.; van Hulst, N. F. *Nat. Photonics* **2007**, *1* (5), 242.
(44) Lee, K. G.; Kihm, H. W.; Kihm, J. E.; Choi, W. J.; Kim, H.; Ropers, C.; Park, D. J.; Yoon, Y. C.; Choi, S. B.; Woo, D. H.; Kim, J.; Lee, B.; Park, Q. H.; Lienau, C.; Kim, D. S. *Nat. Photonics* **2007**, *1* (5), 243–244.
(45) Esteban, R.; Vogelgesang, R.; Dorfmuller, J.; Dmitriev, A.; Rockstuhl, C.; Etrich, C.; Kern, K. *Nano Lett.* **2008**, *8* (10), 3155–3159.
(46) Balanis, C. *Antenna Theory: Analysis and Design*, 2nd ed.; John Wiley & Sons, Inc.: New York, 1997.
(47) Bennett, H. E. Bennett, J. M. *Optical properties and electronic structure of metals and alloys*; North-Holland: New York, 1966.
(48) Stratton, J. A. *Electromagnetic theory*; McGraw-Hill Book Company, Inc.: New York and London, 1941.
(49) Ordal, M. A.; Long, L. L.; Bell, R. J.; Bell, S. E.; Bell, R. R.; Alexander, R. W.; Ward, C. A. *Appl. Opt.* **1983**, *22* (7), 1099–1119.
(50) Johnson, P. B.; Christy, R. W. *Phys. Rev. B* **1972**, *6* (12), 4370.
(51) Gomez-Rivas, J.; Kuttge, M.; Kurz, H.; Haring Bolivar, P.; Sanchez-Gil, J. A. *App. Phys. Lett.* **2006**, *88* (8), 082106.
(52) Canchal-Arias, D.; Dawson, P. *Surf. Sci.* **2005**, *577* (2−3), 95–111.
(53) Ditlbacher, H.; Hohenau, A.; Wagner, D.; Kreibig, U.; Rogers, M.; Hofer, F.; Aussenegg, F. R.; Krenn, J. R. *Phys. Rev. Lett.* **2005**, *95* (25), 257403.

NL900638P